Check for updates

Probing the stoichiometry dependent catalytic activity of nickel selenide counter electrodes in the redox reaction of iodide/triiodide electrolyte in dye sensitized solar cells†

Mildred A. Airo,[*ab] Francis Otieno,[ac] Lineo Mxakaza,[a] Adewale Ipadeola,[a] Rudo S. Kadzutu-Sithole,[a] Lerato F. E. Machogo-Phao,[ad] Caren Billing, [iD][a] Makwena Moloto [iD][b] and Nosipho Moloto [iD][*a]

Nickel selenide (Ni_xSe_y) systems have received much attention in recent years as potential low cost counter electrodes (CEs) in dye sensitized solar cells (DSSCs). Their electrocatalytic activities are comparable to that of the conventional platinum CE. Despite their achievements, the effect of stoichiometry on their catalytic performance as CEs in DSSCs still remains unclear, hence the motivation for this work. Different stoichiometries of Ni_xSe_y were synthesized *via* a colloidal method in oleylamine or oleylamine/oleic acid mixture at the appropriate synthetic temperature and Ni to Se precursor ratio. X-ray diffraction revealed that different stoichiometries of nickel selenide were formed namely, $NiSe_2$, Ni_3Se_4, $Ni_{0.85}Se$, $NiSe$ and Ni_3Se_2. Scanning electron microscopy showed that all the stoichiometries had predominantly spherical-like morphologies. Cyclic voltammetry, electrochemical impedance spectroscopy analysis and the photovoltaic performances of the DSSCs fabricated using the different Ni_xSe_y CEs revealed that selenium rich stoichiometries performed better than the nickel rich ones. Consequently, the catalytic activity towards the redox reaction of the triiodide/iodide electrolyte and hence the power conversion efficiency (PCE) followed the order of $NiSe_2 > Ni_3Se_4 > Ni_{0.85}Se > NiSe > Ni_3Se_2$ with PCE values of 3.31%, 3.25%, 3.17%, 2.35% and 1.52% respectively under ambient conditions.

1. Introduction

The high cost of and low abundance of platinum have hindered its large-scale practical application despite its excellent electro-catalytic activities.[1,2] Moreover, the long-term stability of a Pt counter electrode (CE) can be destroyed in a liquid electrolyte composed of the triiodide/iodide (I^-/I_3^-) redox couple in dye sensitized solar cells (DSSCs). As a result, tremendous efforts are being made to find alternative catalysts to Pt for use as CEs in DSSCs and for electro-catalytic oxygen–hydrogen reduction in fuel cells.[3] This search is geared towards the discovery of inexpensive electrocatalysts that are based on earth abundant elements.[1] For instance, Ni_xSe_y series including NiSe, $NiSe_2$, Ni_3Se_2, Ni_3Se_4 and $Ni_{0.85}Se$ (ref. 4 and 5) and their composites such as graphene/Ni_xSe_y composite[6] and cobalt-doped Ni_xSe_y (ref. 7) have drawn significant attention in the effort to replace Pt as CEs in DSSCs. This is due to their high earth abundance, high electro-conductivity, chemical and thermal stability, and tunable electronic configurations.[6,8] In addition, the strategy of fabricating the CEs with Ni_xSe_y is rather simple and inexpensive hence allowing large-scale production at low cost[5] while simultaneously keeping/improving the performance of DSSCs.

A number of researchers have demonstrated potential utilization of different stoichiometries of Ni_xSe_y nanomaterials on DSSCs as CEs and their performance compare remarkably well with Pt. The function of the CE in DSSCs is to catalyze the redox I^-/I_3^- reaction used as the liquid electrolyte. Thus it is of great importance that the design of the CE material is such that electro-catalytic activity is enhanced just like any other catalyst. Their chemical and surface composition, configuration and the interaction between the different components of the CE material are very critical as they will affect the intrinsic catalytically active sites and the transport properties.[1,9] As a result, much attention has been paid to control the stoichiometry and morphology *via* controlled synthesis techniques of nickel

[a]Molecular Science Institute, School of Chemistry, University of the Witwatersrand, Private Bag 3, Wits, 2050, Republic of South Africa. E-mail: Mildred.Airo@wits.ac.za; Nosipho.Moloto@wits.ac.za; Tel: +27 73 761 0875; +27 11 717 6774

[b]Department of Chemistry, Vaal University of Technology, Private Bag X021, Vanderbijlpark, 1900, Republic of South Africa

[c]Department of Physics, University of the Witwatersrand, Private Bag 3, Wits, 2050, Republic of South Africa

[d]Analytical Services Division, Mintek, 200 Malibongwe Drive, Randburg, South Africa

† Electronic supplementary information (ESI) available. See DOI: 10.1039/d0ra06150f

selenide nanomaterials in order to further enrich the electro-catalytic activity.[5,10]

Many methods including hydrothermal, solvothermal and thin film deposition have been employed to obtained different morphologies and stoichiometries; however, these methods tend to lack real control. The colloidal method has been shown to be effective at controlling the growth and morphology of the nanoparticles and this characterized by quick nucleation, followed by the growth of the nuclei driven mostly by monomer concentration and temperature.[11,12] The colloidal method has two routes of syntheses, one that involves the injection of precursors in a hot solvent and the other that involves quick heating up of precursors in a high boiling solvent from room temperature to the desired temperature and this route is better known as the non-injection synthesis (NIS). There is however scarce information on the NIS of Ni_xSe_y systems. Numerous investigations indicate that precursors used in NIS should have negligible reactivity at low temperatures, but significant reactivity at elevated temperatures because high quality colloidal nanocrystals are produced at relatively high temperature (>200 °C).[13,14] This method has been applied to produce a number of high quality nanocrystals including CdSe, CdTe, PbSe, Ag_2S, Cu_2S, PbS, Ni_3S_4, CdS, ZnS, $CuInS_2$ Cu_2ZnSnS_4 and InSe just to mention a few.[15–19]

As discussed above, catalytic performance of Ni_xSe_y depends on the stoichiometric ratio. Similarly, theoretical calculations for I_3^-/I^- redox process suggest that the metal sites in a metal chalcogenide are more active compared to the chalcogenides sites.[20,21] This implies that the stoichiometric ratio of the metal in the compound largely affect the catalytic activity. This implies that the catalytic activity of the Ni_xSe_y series increases towards the reduction of I_3^- in the order of Ni_3Se_2 < NiSe < $Ni_{0.85}Se$ < Ni_3Se_4 < $NiSe_2$ among other stoichiometries of Ni_xSe_y. However, there are few reports on nickel rich selenides compared to selenium rich ones for DSSC applications. In this present work, different stoichiometries of Ni_xSe_y were synthesized with relatively similar morphologies via the NIS. Synthetic parameters such as temperature, surfactant/co-surfactant and mole ratios of Ni and Se precursors were manipulated to demonstrate how the Ni_xSe_y metastable phases/states largely depend on these parameters. Varying the mole ratio of Ni and Se precursors was aimed at obtaining different Ni content in the sample while temperature was varied to obtain a different stoichiometry at a particular mole ratio. In all cases, oleylamine was used as a reducing and/or stabilizing ligand while oleic acid was used as a co-surfactant in some cases in order to produce different stoichiometry. Systematic analyses of the XRD and XPS among other techniques were done to shed light on the role of the mole ratio and temperature on nanoparticles formation, their structural and chemical composition. Furthermore, the catalytic ability towards the reduction of I_3^- of the different stoichiometries of Ni_xSe_y was investigated to demonstrate the critical role of stoichiometry in CE performance. Finally, DSSCs were fabricated in ambient environment and using cheap dishwashing liquid soap as one of the ingredients in the preparation of TiO_2 paste.

2. Experimental procedures

2.1. Chemicals

Nickel(II) chloride hexahydrate (99.9%), selenium powder (99%), oleylamine (OLA, 70%), oleic acid (OA, 98%), toluene (anhydrous, 99.8%), ethanol (96%), acetone (99.5%), acetylacetone (≥99%), isopropanol (anhydrous, 99.5%), hexane (anhydrous, 95%), lithium perchlorate, lithium iodide (99.99%), iodine (synthetic grade), 4-*tert*-butylpyridine (98%), *N*-methyl-2-pyrrolidone (NMP, anhydrous 99.5%), anatase TiO_2 nanoparticles (<25 nm particle size, 99.7%), acetic acid (99.7%), distilled water, dishwashing liquid (©Sunlight) as an alternative to hydroxypropyl cellulose, N-719 dye (95%), and FTO glass (surface resistivity ~ 7 Ω sq^{-1}); all these were purchased from Sigma Aldrich.

2.2. Synthesis of various nickel selenide nanostructures

Synthesis of NiSe$_2$ (NS-1). About 0.6480 g of $NiCl_2$ and 0.7896 g of Se powder (mole ratio 1 : 2 for $NiCl_2$: Se) were placed in a 50 mL three neck round bottom flask. 10 mL of OLA was added to the flask to act as the solvent, a reducing agent and a capping agent. The mixture was degassed for 20 min then heated quickly to 200 °C under nitrogen and strong magnetic stirring. The reaction was then maintained at this temperature for 30 min after which the reaction was arrested and the contents of the flask were cooled to 80 °C. The black solution was then transferred to centrifuge tubes after which excess of ethanol was added and the solid was isolated by centrifugation. The solid was washed several times with a mixture of ethanol/hexane/toluene in a 1 : 1 : 1 volume ratio and left to dry at room temperature.

Synthesis of Ni$_3$Se$_4$ (NS-2). A similar procedure to the synthesis of $NiSe_2$ including the reaction parameters was followed. However, to obtain a phase change, oleic acid was added as a co-surfactant to oleylamine such that their volume ratio was 1 : 1 (OLA : OA).

Synthesis of Ni$_{0.85}$Se (NS-3). $Ni_{0.85}Se$ synthesis procedure was the same as Ni_3Se_4 however the $NiCl_2$: Se ratio was changed to 1 : 1.

Synthesis of NiSe (NS-4). The synthesis procedure was similar to the synthesis of $NiSe_2$ however the $NiCl_2$: Se mole ratio was changed to 1 : 1.

Synthesis of Ni$_3$Se$_2$ (NS-5). The synthesis procedure was similar to the synthesis of $NiSe_2$ however the reaction temperature was changed to 240 °C and the $NiCl_2$: Se mole ratio to 2 : 1. It is noteworthy to mention that when the temperature was maintained at 200 °C like all the above methods, the obtained product was $Ni_{0.85}Se$. The summary of all the reactions is shown in Table 1.

2.3. Fabrication of counter electrodes

The whole process was performed in a fume hood under ambient conditions. To prepare the counter electrode, 40 mg of the as-prepared Ni_xSe_y nanoparticles were dispersed in 1 mL of NMP in a vial. The mixture was left overnight at room temperature under strong magnet stirring to form a homogeneous ink solution. The as-prepared solution was then sonicated for 10 min after which the solution was drop-casted on pre-cleaned FTO glass substrates then annealed at 100 °C for 10 min. For comparison studies, a reference

Paper

Table 1 Summary of the reaction conditions for the synthesis of Ni_xSe_y

Sample	Reaction
NS-1	$NiCl_2(1\ mol) + Se(2\ mol) \xrightarrow[\triangle\,200\ °C]{OLA} NiSe_2$
NS-2	$NiCl_2(1\ mol) + Se(2\ mol) \xrightarrow[\triangle\,200\ °C]{OLA/OA} Ni_3Se_4$
NS-3	$NiCl_2(1\ mol) + Se(1\ mol) \xrightarrow[\triangle\,200\ °C]{OLA/OA} Ni_{0.85}Se$
NS-4	$NiCl_2(1\ mol) + Se(1\ mol) \xrightarrow[\triangle\,200\ °C]{OLA} NiSe$
NS-5	$NiCl_2(2\ mol) + Se(1\ mol) \xrightarrow[\triangle\,240\ °C]{OLA} Ni_3Se_2$

platinum CE was prepared by sputter-coating a thin layer of Pt (200 nm) to a clean FTO substrate.

2.4. Preparation of TiO₂ paste

The preparation was adopted from previously reported work.[22,23] Specifically, 1 g of commercially purchased anatase TiO₂ powder was mixed with 12 mL distilled water and 0.5 mL acetylacetone under constant magnetic stirring for 24 h. The mixture was later dried at 60 °C followed by grinding to a fine powder. This initial stage was carried out to prevent reaggregation of the TiO_2 nanoparticles. The subsequent stage involved the mixing of one drop of dishwashing liquid soap (in place of 5% (w/v) ethanolic solution of hydroxypropyl cellulose), 0.2 mL acetic acid and 3 mL of ethanol with the pre-treated TiO_2 powder under constant stirring for 12 hours. The solution was heated afterwards at 70 °C with constant stirring to evaporate ethanol slowly.

2.5. Fabrication of the photoanode

The nanocrystalline TiO_2 paste was printed on a clean FTO substrate *via* a doctor blade technique after which the films were annealed at 450 °C for 30 min. The aim of the heat treatment was to remove all the residual organic components/chemicals from the TiO_2 surface as well as to get an improved
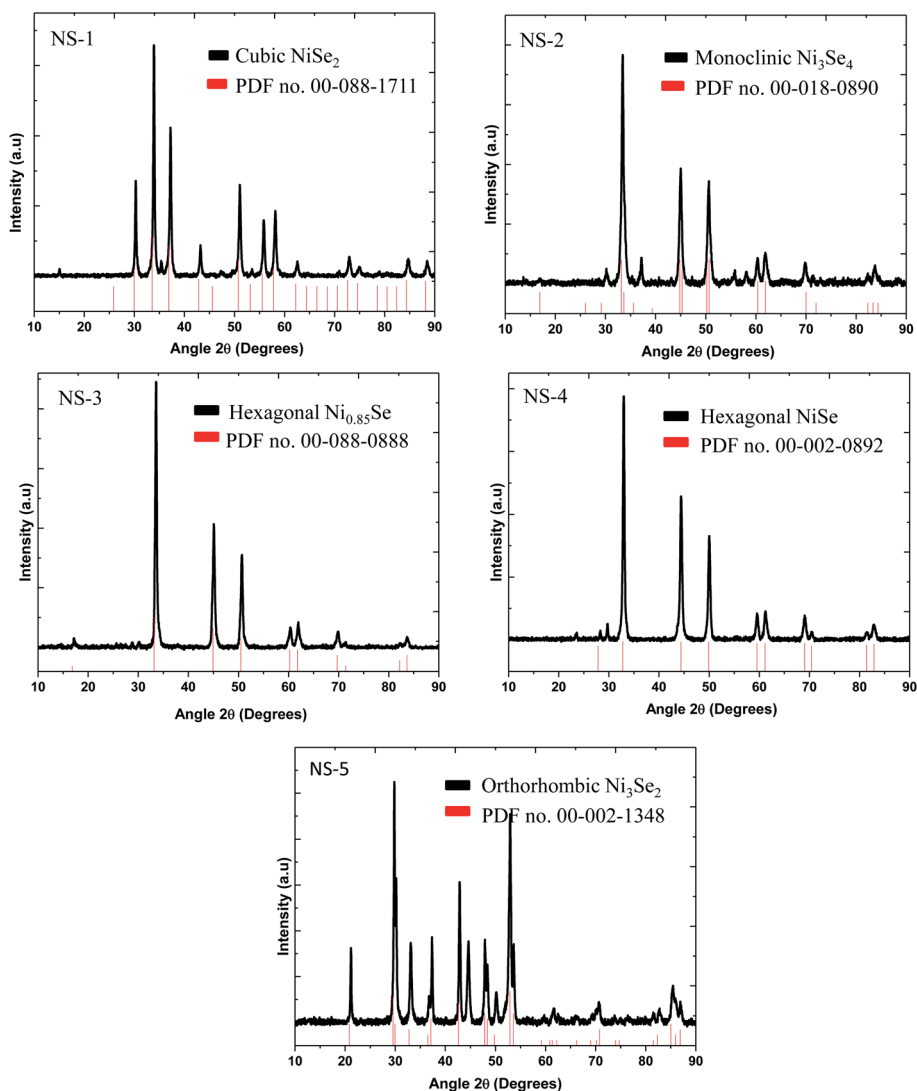
Fig. 1 X-ray diffraction patterns of NS-1, NS-2, NS-3, NS-4 and NS-5.

contact with the TiO_2 aggregates, and between the TiO_2 and dye molecules. The thickness and the active area of the TiO_2 films were approximately 200 nm and 0.25 cm^2 respectively. For sensitization, the TiO_2 films were immersed in a dye solution (3.0×10^{-4} M mixture of the ruthenizer 535-bisTBA (N-719) in methanol) for 5 s then left to dry for 12 h. All this were done at room temperature.

2.6. Device assembly

Finally, the DSSC device was assembled according to the following method. The photoanode was placed face up on a flat surface, and the Ni_xSe_y coated counter electrode was placed on top of the photoanode. These two opposing glass plates were offset from one another so that the entire photoanode was covered by the counter electrode. The redox electrolyte solution (I^-/I_3^-), composed of 0.05 M iodine, 0.5 M *tert*-butylpyridine, and 0.1 M lithium iodide, 0.1 M potassium iodide, 0.1 M sodium iodide was placed at the edges of the plates, and the liquid was drawn into the space between the electrodes *via* capillary action. An epoxy adhesive was utilized to hold/seal the electrodes together. Accordingly, we fabricated the NiSe, $Ni_{0.85}Se$ $NiSe_2$, Ni_3Se_4, Ni_3Se_2 and Pt (as a reference device) counter electrode-based DSSCs.

3. Characterization techniques

3.1. Structural characterization

The phase purity, crystallinity and preferred crystal orientation of the products were examined using X-ray diffraction (XRD) on a Bruker MeasSrv (D2-205530)/D2-205530 diffractometer using secondary graphite monochromated CuK_α radiation (λ 1.5418 Å) at 30 kV/30 mA. Measurements were taken using a glancing angle of incidence detector at an angle of $2°$, for 2θ values between $10–90°$ in steps of $0.026°$ with a step time of 37 s and at a temperature of 25 °C.

The sample morphologies were determined by scanning electron microscopy (SEM) analysis using an FEI Nova Nanolab 600 FIB/SEM instrument operating at 30 kV. The film morphologies and structures were characterized using Veeco Di-3100 atomic force microscopy (AFM) in the tapping mode.

3.2. Electrochemical studies

The extent of the electrocatalytic activities of the Ni_xSe_y CE materials were determined using cyclic voltammetry (CV), electrochemical impedance spectroscopy (EIS) and Tafel polarization measurements using an electrochemical workstation (Biologic: VMP 300). The CV measurements were carried out in a three-electrodes cell with an anhydrous acetonitrile (ACN) solution containing 0.01 M LiI, 0.001 M I_2 and 0.1 M $LiClO_4$ as the I^-/I_3^- redox electrolyte at a scan rate of 100 mV s^{-1}, using Pt as the counter electrode, Ag/AgCl as the reference electrode and the fabricated Ni_xSe_y as the working electrodes. The EIS measurements were analysed using a symmetric cell assembled with two FTO glass substrates coated with an identical counter electrode in the redox electrolyte used for DSSCs in the dark. The samples were tested between 100 kHz and 100 mHz at open

circuit potential 0.6 V. The Tafel polarization measurements were carried out using the symmetric cell assembly at potential window of 0.0 to 1.0 V and a scan rate of 100 mV s^{-1}.

3.3. Photovoltaic measurements

The photovoltaic test for the DSSCs with an active area of 0.25 cm^2 was carried out by measuring the photocurrent–voltage (*J–V*) characteristic curves using a HP 4141B source measure unit (SMU). All the measurements were carried out in ambient conditions. The incident light intensity was controlled at 70 mW cm^{-2} (AM 1.5G).

4. Results and discussion

4.1. Characterization of the nickel selenide nanostructures

The crystalline phases of the as-synthesized products were characterized using powder X-ray diffraction and the results are shown in Fig. 1. The NS-1 sample was indexed to cubic $NiSe_2$ based on PDF no. 011-088-1711 while NS-2 matched to the monoclinic Ni_3Se_4 according to PDF no. 00-018-0890. This phase change was observed when OA was used as a co-surfactant to OLA. The NS-3 sample gave hexagonal $Ni_{0.85}Se$
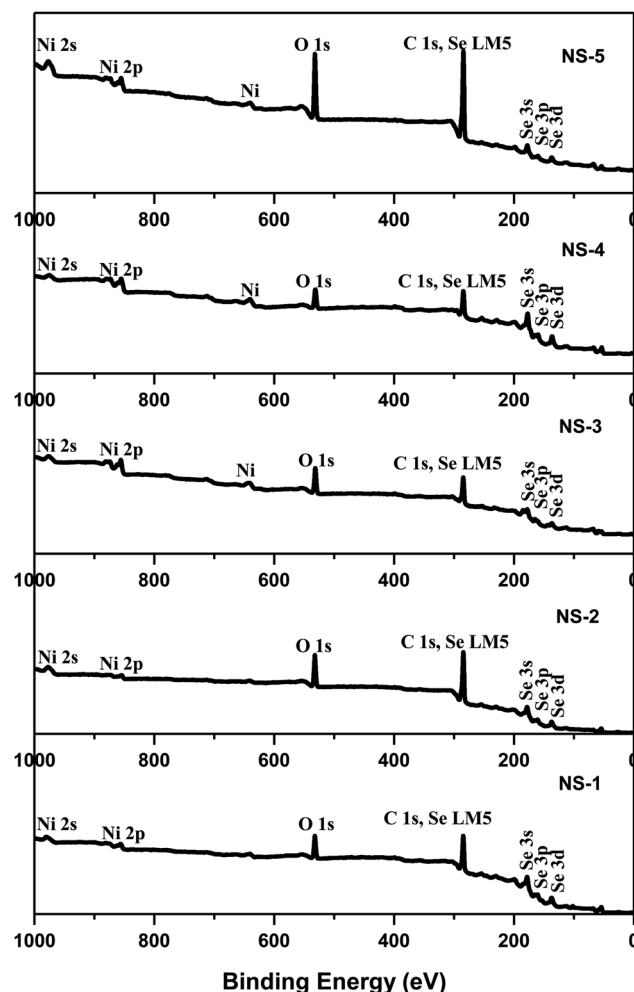
Fig. 2 Survey spectra of NS-1, NS-2, NS-3, NS-4 and NS-5.
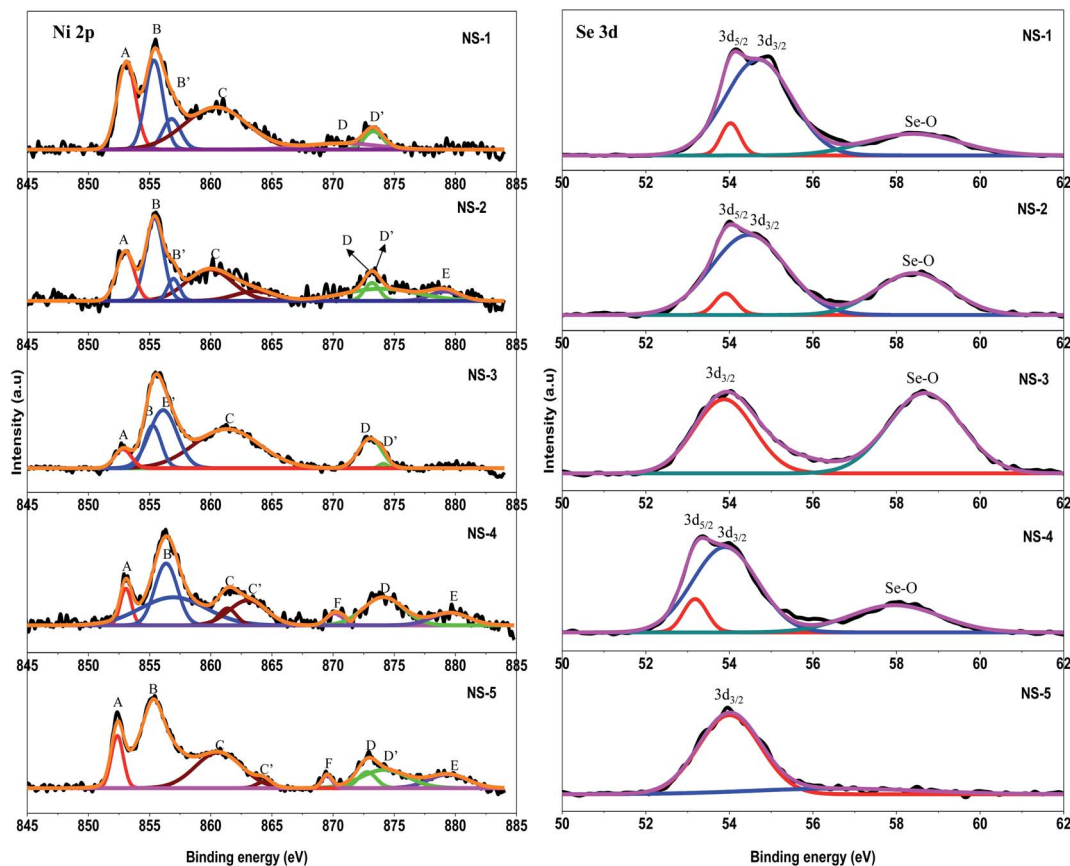
Fig. 3   Ni 2p and Se 3d high resolution XPS spectra of NS-1, NS-2, NS-3, NS-4 and NS-5.

with equivalent peaks matching to those of PDF no. 00-018-0888 while the pattern for NS-4 predominantly matched hexagonal-NiSe of PDF no. 00-002-0892. Finally, the NS-5 was matched to an orthorhombic Ni_3Se_2 PDF no. 00-002-1348. This confirms that by merely changing a few parameters, different stoichiometries of nickel selenide can be synthesized.

X-ray photoelectron spectroscopy (XPS) is a useful technique to evaluate the surface chemistry as well as the bonding in the resultant particles. The XPS survey spectra of the as-synthesized nanoparticles show the expected elemental compositions and the respective binding energies. Shown in Fig. 2 are the survey spectra of the nickel selenide samples. All the samples showed the presence of Ni, Se, C and O. The C is due to the capping agent and O is to a large extent due to the surface oxidation of the capping agent and the lesser extent, the particles.[24,25]

For more insight on the surface composition and valence state/chemical state of the as-synthesized nanostructures, high resolution XPS scans of nickel and selenium were done and the results are shown in Fig. 3. The Ni 2p spectra for all the samples showed multiple peaks, the doublets $2p_{3/2}$ and $2p_{1/2}$ owing to the spin orbital coupling and shake-up satellite peaks.[26,27] The results are summarized in Table 2.

All the samples showed an A peak at ~853 eV which was attributed Ni^{3+} shakeup satellite peak. The B and B′ peaks were attributed to the Ni $2p_{3/2}$ doublet where the peak at ~855 eV was assigned to Ni^{2+} and the peak at ~856 eV to Ni^{3+}. The D and D′ peaks were attributed to the Ni $2p_{1/2}$ state where the peak at ~873 eV is attributed Ni^{2+} and the peak at ~874 eV to Ni^{3+} respectively.[26,27] The rest of the peaks assigned to shakeup satellite peaks were shifted by ~5 eV (C) and ~8 eV (C′) from

Table 2   Summary of the deconvoluted peaks in the high resolution Ni 2p spectra of NS-1, NS-2, NS-3, NS-4 and NS-5

Sample	A (eV)	B (eV)	B′ (eV)	C (eV)	C′ (eV)	D (eV)	D′ (eV)	E (eV)	F (eV)
NS-1	853.09	855.37	856.80	860.43	—	873.42	—	—	870.71
NS-2	853.12	855.40	856.95	859.90	864.02	873.18	873.91	879.12	—
NS-3	853.06	855.36	856.10	861.30	—	873.04	874.10	—	—
NS-4	853.11	855.43	856.14	860.37	863.49	873.31	—	878.78	870.70
NS-5	852.35	855.32	—	860.87	864.36	872.80	874.20	879.40	869.30

Table 3 High resolution Se 3d spectra of NS-1, NS-2, NS-3, NS-4 and NS-5

Sample	$3d_{5/2}$ (eV)	$3d_{3/2}$ (eV)	Se–O (eV)
NS-1	54.0	54.7	58.4
NS-2	53.9	54.5	58.4
NS-3	—	53.9	58.7
NS-4	53.4	54.0	58.0
NS-5	—	54.0	—

Ni^{2+} ($2p_{3/2}$) and Ni^{3+} ($2p_{3/2}$) respectively while E and F were shifted by ∼3 eV and ∼5 eV from Ni^{2+} ($2p_{1/2}$) and Ni^{3+} ($2p_{1/2}$) correspondingly. The appearance of double peak features of Ni (2p) along with their consecutive shake-up satellite peaks were indicative of the magnetic chemical state of Ni^{2+} and Ni^{3+} state.[28] These observations confirm that the peak positions were similar to those reported in previous studies for the presence of Ni^{2+} and Ni^{3+} oxidation states in both stoichiometric and non-stoichiometric Ni_xSe_y.[29,30] Nevertheless, when studying the area under the peaks it was evident that the Ni^{2+} oxidation state was dominant in samples NS-1, NS-2, NS-3 and NS-5. This is not surprising as the +2 oxidation state is the most stable. The high resolution Se 3d spectra are shown in Fig. 3 and the assignments are summarized in Table 3. Largely, two peaks were observed for all samples except NS-5. The first peak was deconvoluted to two bands corresponding to $3d_{5/2}$ and $3d_{3/2}$ peaks and the second peak was associated with surface oxidation of selenium resulting in formation of SeO_2.

On the basis of XPS, especially the Se 3d analysis, it was clear that the series of nickel selenide compounds exhibited adjustable binding energies achieved by possibly varying the nickel content in the Ni–Se framework. To illustrate this, the $3d_{5/2}$ band which was the predominant peak in all the samples was seen to red-shift from that of neutral Se ($3d_{5/2}$ at 55.1 eV) by 0.4, 0.6, 1.2, 1.1 and 1.1 eV in NS-1, NS-2, NS-3, NS-4 and NS-5 respectively. The degree of the red-shifting could be attributed to the different binding interaction experienced by Se^{2-} anion

with the different metal cation present in the sample. In addition, NS-3 that exhibited predominantly Ni^{3+} ion was seen to experience high level of oxide on the selenium surface while the metal rich NS-5 did not have any surface oxide peak.

SEM was used to analyse the morphology of the nanostructures. Generally, the use of OLA alone as a surfactant mostly supported thermodynamic growth such that nanospheres were predominantly obtained throughout all the samples as shown in Fig. 4. Some evidence of rod-like formation was also observed as in samples NS-3, NS-4 and NS-5. Nevertheless, the particles were largely spherical. Following the characterization Ni_xSe_y nanostructures, the particles were then used to fabricate thin films which were to be used as CEs. The AFM images are shown in Fig. 5. The topography of the films suggested that the morphology of the nanostructures on the film were spherical-like for all the samples, thus confirming observations made by SEM. The root mean square (rms) roughness values were 413 nm, 249 nm, 250 nm, 410 nm and 396 nm for NS-1, NS-2, NS-3, NS-4 and NS-5 respectively while rms for the sputter coated Pt was 4 nm. The roughness could have an effect on the electrocatalysis activity but moreover it has been shown to affect solar cell performance due to interfacial losses.[31]

4.2. Application of the nickel selenide nanostructures as counter electrodes in dye sensitized solar cells

CV measurements were carried out to determine the reaction kinetics of the nickel selenide CE materials in a three-electrode system. For comparison purposes, the CV characterization of the Pt film-CE was performed under the same conditions and the results are presented in Fig. 6. Two pairs of redox peaks were observed on the CV curves with similar shapes for all of the CEs. This suggested that Ni_xSe_y CEs had relatively similar electrochemical stability and catalytic activity during the redox process. The redox peaks at lower potential were attributed to oxidation and reduction reactions which are represented by eqn (1) and the redox couple at higher potential peaks corresponded to the reaction represented by eqn (2).[21,32]

$$I_3^- + 2e^- \leftrightarrow 3I^- \tag{1}$$
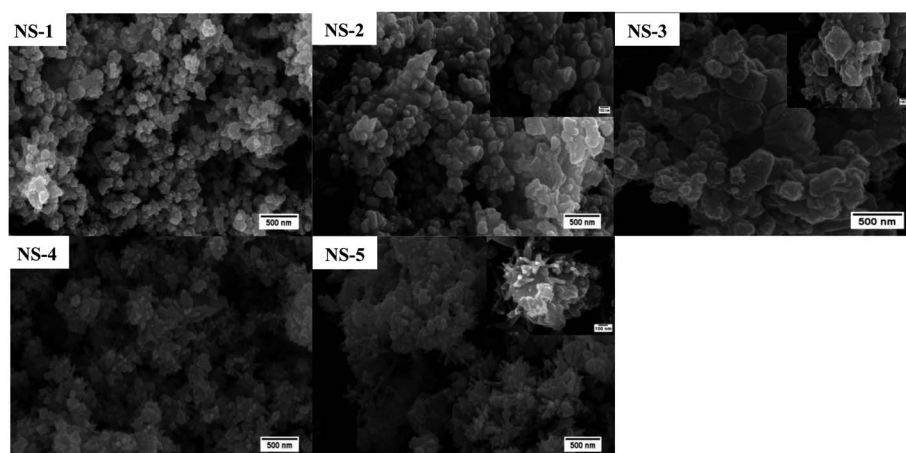
Fig. 4 SEM images of NS-1, NS-2, NS-3, NS-4 and NS-5.
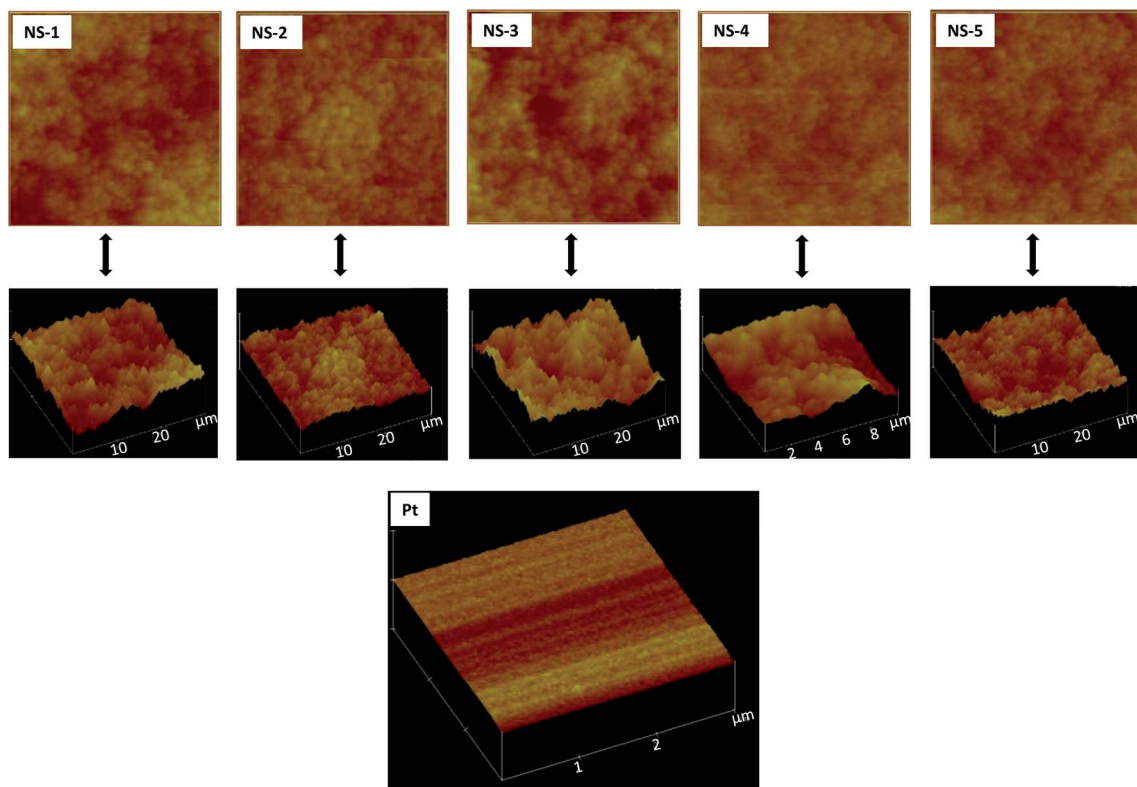
Fig. 5 AFM images of NS-1, NS-2, NS-3, NS-4 and NS-5.

$$3I_2 + 2e^- \leftrightarrow 3I_3^- \qquad (2)$$

The peak-to-peak separation (E_{pp}) between the first reduction peak ($J_{\_Red-1}$) and oxidation peak also corresponds to the reversibility of the redox reaction. The electrocatalytic ability of the CE for the reduction of I_3^- in DSSCs can be visualized based on the cathodic/reduction peak current density and peak to peak potential E_{pp}. Generally, the stronger the electrocatalytic

ability, the larger $|J_{\_Red-1}|$ and lower E_{pp} values.[2,7,33] As shown in Fig. 6 and Table 4, most of the Ni_xSe_y CEs exhibited superior current response (J) than the Pt-CE for the reduction of I_3^- in order of NS-1 > NS-2 > NS-3 > Pt > NS-4 > NS-5, indicating that the rate of this reaction is relative higher for the NS-1, NS-2, NS-3 than the Pt. Whereas the E_{pp} for all the catalyst recorded approximately the same value ($\sim$0.7 V) which was a clear indication that the same amount of energy was required for this reaction by all the catalysts. The above observations suggest that the electrocatalytic activity of Ni_xSe_y CEs can be changed by controlling the stoichiometry of the nickel selenide. The long-term stability of DSSCs is one of the most important photovoltaic parameters and can be reflected by the consecutive CV scans. To demonstrate the stability of Ni_xSe_y in the iodine electrolyte and their reliability as counter electrodes, several scans of CV measurements were done and the results depicted in Fig. S2.† Again here, the Pt was used as control. The results confirmed that the as-prepared counter electrodes exhibited an excellent chemical stability in the electrolyte solution with little degradation in current densities or peak shifts after 30 scans at 50 mV s^{-1}.

EIS was employed to probe the charge transfer ability between the Ni_xSe_y CEs and the electrolyte. This was conducted on symmetrical dummy cells with two identical electrodes sandwiching the I_3^-/I^- electrolyte under dark conditions. Fig. 7 shows the Nyquist plots (Fig. 7B) of the corresponding symmetrical cells with the electrochemical equivalent circuit (Fig. 7A), whose components represent four impedance
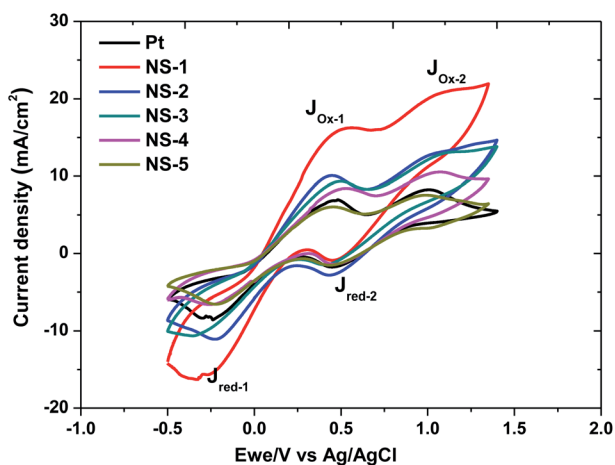
Fig. 6 Cyclic voltammograms for the Ni_xSe_y and Pt counter electrodes with a scan rate of 100 mV s^{-1}.

Table 4 Electrical parameters derived from the CV, EIS and Tafel polarization curves

CE	E_{pp}	CV J_{sc} (mA cm^{-2})	R_s (ohm)	R_{ct} (ohm)	Log J_0 (mA cm^{-2})	Log J_{lim} (mA cm^{-2})
Pt	0.69	8.14	135.90	7.56	−2.77	−2.41
NS-1	0.71	15.32	139.90	37.35	−3.16	−2.74
NS-2	0.68	10.98	145.2	46.62	−3.56	−2.89
NS-3	0.72	10.31	185.2	64.69	−3.70	−3.11
NS-4	0.69	6.13	315.1	262.1	−4.07	−3.49
NS-5	0.68	6.10	186.0	151.6	−4.31	−3.69

properties where R_s signifies the series resistance, which includes the transport resistance, bulk resistance of the CEs, and contact resistance of cells thus explaining the resistance of the CE to the electrolyte; R_{ct} denotes the charge transfer resistance at the CE/electrolyte interface, which shows the transport properties and conductivity at the CE/electrolyte interface; C_{dl} which corresponds to the double layer capacitance which is employed when a perfect semi-circle is obtained from the Nyquist plot and explains the charge storage capacity of the CEs; and Z_w represents the Nernst diffusion element, often employed when a line is at 45° to the semi-circle at lower frequency region and explains if the interaction between the CE and the electrolyte is diffusion-controlled.[34]

The two key parameters, R_s and R_{ct}, obtained using the Z-fit in EC-Chem software from Biologic is summarized in Table 4. The R_s value for Pt was smaller than those of Ni$_x$Se$_y$ CEs meaning that it was more conductive as R_s is dependent on conductivity.[7,20] The higher R_s values of Ni$_x$Se$_y$ CEs in comparison to Pt was attributed to the rough inhomogeneous surface of the films as portrayed in the AFM analysis; and the poor adhesion of the Ni$_x$Se$_y$ inks on the FTO substrate.[7,35] The recombination resistance, $(R_s + R_{ct})$ derived from the values in Table 4 revealed that among the Ni$_x$Se$_y$ CEs, NS-1 (177.25 Ω) had the closest $R_s + R_{ct}$ value to that of Pt (143.46 Ω), meaning that its conductivity is comparable to Pt and it was the most conductive of the Ni$_x$Se$_y$ CEs in this study. This can be explained by the fact that cubic NiSe$_2$ is considered to be more metallic.[36] This is in agreement with the CV results that showed the conductivity and electrons transport properties of NS-1 were comparable to those of Pt. NS-2 and NS-3 then followed possibly because of the two active Ni species in the form of Ni^{2+} and Ni^{3+}. The observable difference in the R_s value between NS-3 and NS-4 may have resulted from the fact that the surface of the NS-4 was highly oxidized as was portrayed by prominent presence of SeO$_2$ in the Se 3d XPS spectrum thus inhibiting electron movement. The nickel rich NS-5 was forth while NS-4 believed to be a semiconductor[25] had the lowest conductivity suggested by the highest R_s value recorded herein. The charge transfer process represented by the diameter of the semicircle on the high frequency region reflecting on the R_{ct} value followed the same sequence as the R_s for the Ni$_x$Se$_y$ CEs for the same reasons already explained. However, the values were relatively larger compared to that of Pt indicating slightly sluggish charge transfer kinetics. Therefore, comparing the values of R_s and R_{ct}, it was concluded that the superiority of the electrocatalytic activity of Ni$_x$Se$_y$ CEs for I$_3^-$ reduction increased in the order of NS-1 > NS-2 > NS-3 > NS-5 > NS-4.

The symmetric dummy cells used in EIS measurement were employed to further elucidate the catalytic activity of the Ni$_x$Se$_y$ by Tafel polarization curves and the results are presented in Fig. 8. Kinetics surrounding the catalytic activities of CEs are largely dependent on the exchange current density J_0 and the limiting diffusion current density, J_{lim}. From the curves, the J_0 and the J_{lim} can be derived from the slope for anodic or cathodic branch and the intersection of anodic branch with y axis respectively.[2,37] As summarized in Table 4, the values of J_0 and J_{lim} increased in a following order: Pt < NS-1 < NS-2 < NS-3 < NS-5 < NS-4 which is similar to the EIS order. Usually the J_0 value increases with increasing slope of cathodic or anodic branches and eqn (3) suggest that J_0 is inversely proportional to R_{ct}. Therefore, J_0 has correlation with the electrocatalytic activity of the CE, meaning a large J_0 value implies a much better catalytic activity. Similarly, larger J_{lim} value indicates the larger diffusion coefficient D value, which can result to the higher catalytic activity based on eqn (4).

$$J_0 = RT/nFR_{ct} \tag{3}$$

$$J_{lim} = 2nFDC/l \tag{4}$$

where R is the gas constant, T is the temperature (298 K), F is Faraday's constant, n ($n = 2$) is the number of electrons, R_{ct} charge transfer resistance, D diffusion coefficient, C is the concentration of I$_3^-$, and l is the spacer thickness.[4] The deductions derived from the Tafel and EIS as well as CV data analysis are consistent, thus, for the Ni$_x$Se$_y$ CEs herein, NS-1 (NiSe$_2$) is a best electrocatalyst followed by NS-2 (Ni$_3$Se$_4$) and NS-3 (Ni$_{0.85}$Se). This is a possible explanation as to why there is so much literature on the use of NiSe$_2$ (ref. 38 and 39) and Ni$_{0.85}$Se as CEs compared to those of NS-5 (Ni$_3$Se$_2$) and NS-4 (NiSe). In addition, the electrocatalytic ability and charge-transferability of the Ni$_x$Se$_y$ CEs can be changed by controlling the Ni content from 0.5 to 1.5. Therefore, the electrocatalytic activity of the Ni$_x$Se$_y$ CEs varies with the change in Ni content which plays a big role on the conductivity of the material.

4.3. Photovoltaic performance of DSSCs

The Ni$_x$Se$_y$ CEs were then used a in a DSSCs. Fig. 9 shows the comparison of current density–voltage (J–V) characteristics of the devices fabricated from Ni$_x$Se$_y$ as CEs to evaluate the effect of the different stoichiometries. Herein, only the device performances at incident light intensity controlled at 70 mW cm^{-2} (AM 1.5G) are reported since the attempts to use higher power resulted in S-shaped curves (Fig. S1†) and this is
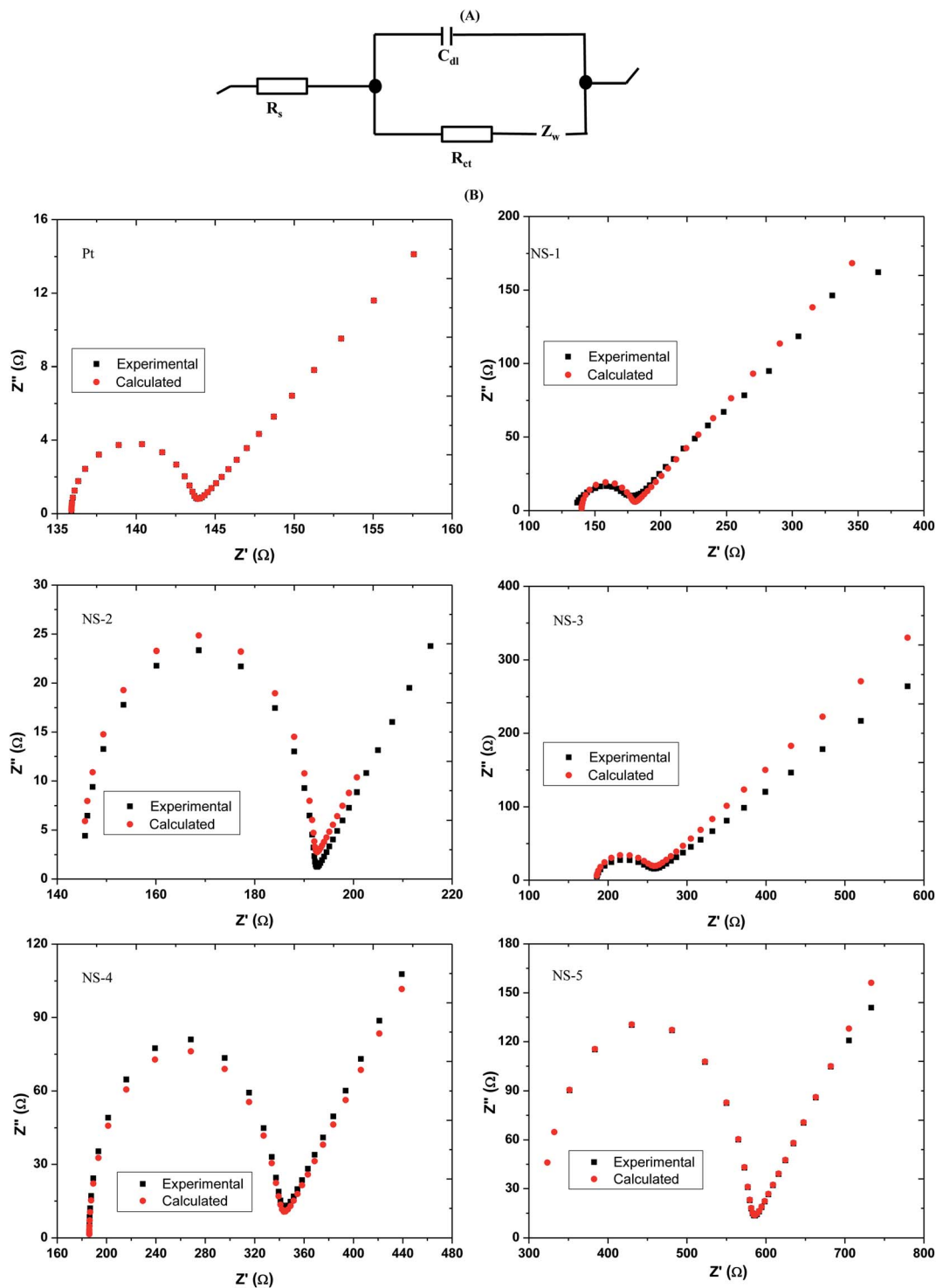
Fig. 7 (A) Electrochemical equivalent circuit and (B) Nyquist plots of EIS for the symmetrical cell with Ni_xSe_y electrodes.

attributed to devices exposure to air. The detailed photovoltaic parameters including the open circuit voltage (V_{oc}), short circuit current density (J_{sc}), fill factor (FF) and power conversion efficiency (PCE) are shown in Table 5. It was observed that the compositions of nickel selenides had some effect on the performance of DSSCs such that NS-1 yielded the highest efficiency of 3.3% and J_{sc} of 10.4 mA cm^{-2}. Overall, the

efficiency of the DSSCs was in the order of Pt > NS-1 > NS-2 > NS-3 > NS-4 > NS-5. Comparing NS-1 to Pt DSSC performance, it was noted that the current density generated by NS-1 (10.4 mA cm^{-2}) was relatively close to that of Pt DSSC (10.5 mA cm^{-2}). However, the FF of all the Ni_xSe_y based CEs was lower than that of the Pt possibly due to the larger R_s encountered
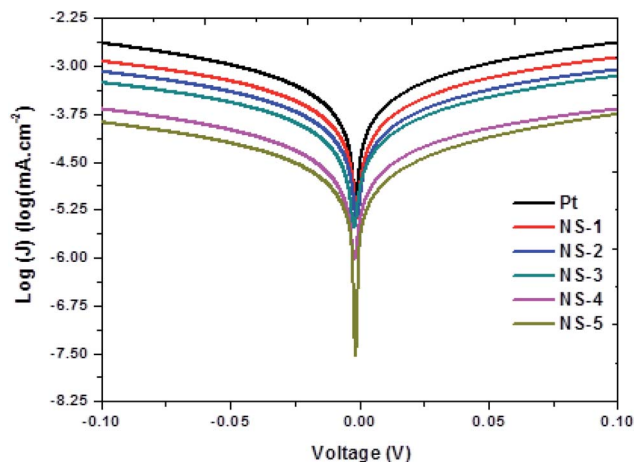
Fig. 8 Tafel polarization curves of the symmetric dummy cells from NS-1 to NS-5, and Pt CEs.

with these CEs as a result of weak adhesion of the nano-structures on FTO.[2,40]

The values of the V_{oc} of all the as-synthesized CEs including Pt were seen to be relatively the same, about 0.7 V. This can be attributed to the fact that the V_{oc} across a DSSC is thermo-dynamically determined by the difference between the quasi-Fermi level of the semiconductor (TiO_2) and the redox poten-tial of the electrolyte.[41] Thus the value of the V_{oc} is independent to the nature of the counter electrode material but dependent on the charge recombination and electron injection efficiency. In addition, the efficiency of DSSCs herein was majorly affected by the increase in J_{sc} of the device. Previous reports indicate that the larger the J_{sc} value the higher the generation of the iodide ions thus the higher the catalytic activity of the CE material.[2,7] Therefore, based on the above observations, NS-1 was a better electrocatalyst towards the reduction of triiodide ion while NS-5 was the weakest. Similarly, the device with NS-1 CE exhibited stronger charge separation and transferability compared to the other stoichiometries, thus the high J_{sc} it generated. In
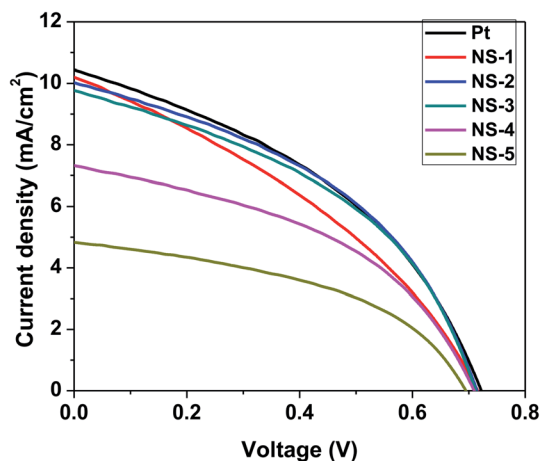
Table 5 DSSCs parameters using Ni_xSe_y as counter electrodes

CE	DSSC J_{sc} (mA cm^{-2})	V_{oc} (V)	FF (%)	PCE (%)
Pt	10.51	0.72	47.30	3.58
NS-1	10.35	0.71	45.01	3.31
NS-2	10.05	0.71	45.64	3.25
NS-3	9.75	0.71	45.80	3.17
NS-4	7.31	0.71	45.40	2.35
NS-5	4.86	0.69	45.32	1.52

summary, the photovoltaic performance of the Ni_xSe_y based CEs suggested that NS-1 ($NiSe_2$), which is a selenium rich stoichiometry presented better efficiency than the metal rich NS-5 (Ni_3Se_2) stoichiometry. The sequence was such that when the metal content increased in the composition, the efficiency value dropped. As such, in terms of device performance, the following trend was observed; NS-1($NiSe_2$) > NS-2 (Ni_3Se_4) > NS-3 ($Ni_{0.85}Se$) > NS-4 ($NiSe$) > NS-5 (Ni_3Se_4). This trend was consistent with observations made in the CV, EIS and Tafel plot analyses.

5. Conclusion

In summary, different stoichiometries of nickel selenide nanostructures (Ni_xSe_y) were successfully synthesized *via* the colloidal method by simply manipulating synthetic parameters (surfactant and temperature). Similar morphologies of nano-spheres were obtained. Stoichiometry was shown to affect the electrocatalytic activity of nickel selenide and thus their photovoltaic performance in a DSSC. In particular, the selenium rich nickel selenide showed better electrocatalytic activity and high efficiency than the nickel rich one (Ni_3Se_2). As the nickel content increased, the efficiency of the device was seen to decrease such that $NiSe_2$ ($Ni_{0.5}Se$) had 3.31%, Ni_3Se_4 ($Ni_{0.75}Se$) had 3.25%, $Ni_{0.85}Se$ had 3.17%, $NiSe$ had 2.35% and Ni_3Se_2 ($Ni_{1.5}Se$) had 1.52% efficiency.

Conflicts of interest

There are no conflicts to declare.

Acknowledgements

References

1 F. Wang, Y. Li, T. A. Shifa, K. Liu, F. Wang, Z. Wang, P. Xu, Q. Wang and J. He, Selenium-enriched nickel selenide nanosheets as a robust electrocatalyst for hydrogen generation, *Angew. Chem., Int. Ed.*, 2016, **55**, 6919–6924.

2 Q. Jiang, R. Chen, H. Chen, J. Jiang, X. Yang, Y. Ju, R. Ji and Y. Zhang, Improved performance in dye-sensitized solar cells

Fig. 9 I–V characteristic of solar cell devices fabricated using different Ni_xSe_y as CEs.

via controlling crystalline structure of nickel selenide, *J. Mater. Sci.*, 2018, **53**, 7672–7682.

3 J. Greeley, T. F. Jaramillo, J. Bonde, I. Chorkendorff and J. K. Nørskov, Computational high-throughput screening of electrocatalytic materials for hydrogen evolution, *Mater. Sustainable Energy*, 2011, 280–284.

4 X. Qian, H. Li, L. Shao, X. Jiang and L. Hou, Morphology-tuned synthesis of nickel cobalt selenides as highly efficient Pt-free counter electrode catalysts for dye-sensitized solar cells, *ACS Appl. Mater. Interfaces*, 2016, **8**, 29486–29495.

5 C.-T. Lee, J.-D. Peng, C.-T. Li, Y.-L. Tsai, R. Vittal and K.-C. Ho, Ni_3Se_4 hollow architectures as catalytic materials for the counter electrodes of dye-sensitized solar cells, *Nano Energy*, 2014, **10**, 201–211.

6 X. Zhang, M. Zhen, J. Bai, S. Jin and L. Liu, Efficient NiSe-Ni_3Se_2/graphene electrocatalyst in dye-sensitized solar cells: the role of hollow hybrid nanostructure, *ACS Appl. Mater. Interfaces*, 2016, **8**, 17187–17193.

7 Q. Jiang, K. Pan, C.-S. Lee, G. Hu and Y. Zhou, Cobalt-nickel based ternary selenides as high-efficiency counter electrode materials for dye-sensitized solar cells, *Electrochim. Acta*, 2017, **235**, 672–679.

8 X. Zhang, J. Bai, B. Yang, G. Li and L. Liu, Self-assembled mesoporous $Ni_{0.85}Se$ spheres as high performance counter cells of dye-sensitized solar cells, *RSC Adv.*, 2016, **6**, 58925–58932.

9 J. Zhuo, M. Cabán-Acevedo, H. Liang, L. Samad, Q. Ding, Y. Fu, M. Li and S. Jin, High-performance electrocatalysis for hydrogen evolution reaction using Se-doped pyrite-phase nickel diphosphide nanostructures, *ACS Catal.*, 2015, **5**, 6355–6361.

10 F. Gong, X. Xu, Z. Li, G. Zhou and Z.-S. Wang, $NiSe_2$ as an efficient electrocatalyst for a Pt-free counter electrode of dye-sensitized solar cells, *Chem. Commun.*, 2013, **49**, 1437–1439.

11 N. Moloto, M. J. Moloto, N. J. Coville and S. Sinha Ray, Optical and structural characterization of nickel selenide nanoparticles synthesized by simple methods, *J. Cryst. Growth*, 2009, **311**, 3924–3932.

12 N. Moloto, M. J. Moloto, N. J. Coville and S. Sinha Ray, Synthesis and characterization of nickel selenide nanoparticles: size and shape determining parameters, *J. Cryst. Growth*, 2011, **324**, 41–52.

13 Y. A. Yang, H. Wu, K. R. Williams and Y. C. Cao, Synthesis of CdSe and CdTe nanocrystals without precursor injection, *Angew. Chem.*, 2005, **117**, 6870–6873.

14 Y. C. Cao and J. Wang, One-pot synthesis of high-quality zinc-blende CdS nanocrystals, *J. Am. Chem. Soc.*, 2004, **126**, 14336–14337.

15 H. Zhong, S. S. Lo, T. Mirkovic, Y. Li, Y. Ding, Y. Li and G. D. Scholes, Noninjection gram-scale synthesis of monodisperse pyramidal $CuInS_2$ nanocrystals and their size-dependent properties, *ACS Nano*, 2010, **4**, 5253–5262.

16 K. P. Mubiayi, D. M. G. Neto, A. Morais, H. P. Nogueira, T. Emílio de Almeida Santos, T. Mazon, N. Moloto, M. J. Moloto and J. N. Freitas, Microwave assisted synthesis of $CuInGaSe_2$ quantum dots and spray deposition of their composites with graphene oxide derivatives, *Mater. Chem. Phys.*, 2020, **242**, 122449.

17 M. A. Airo, S. Gqoba, M. P. Kalenga, S. Govindraju, M. J. Moloto and N. Moloto, Synthesis and characterization of indium monoselenide nanosheets: A proposed pseudo top-down mechanism, *J. Cryst. Growth*, 2014, **406**, 1–7.

18 M. A. Airo, S. Gqoba, F. Otieno, M. J. Moloto and N. Moloto, Structural modification and band-gap crossover in indium selenide nanosheets, *RSC Adv.*, 2016, **6**, 40777–40784.

19 X. Wang, Y. Xie, B. Bateer, K. Pan, Y. Zhou, Y. Zhang, G. Wang, W. Zhou and H. Fu, Hexagonal FeS nanosheets with high-energy (001) facets: counter electrode materials superior to platinum for dye-sensitized solar cells, *Nano Res.*, 2016, **9**, 2862–2874.

20 X. Wang, Y. Xie, K. Pan, J. Wu, Y. Xiao, P. Yu, W. Zhou and H. Fu, Morphology Effect of NiSe hierarchical microspheres on the performance of dye-sensitized solar cells, *ACS Appl. Nano Mater.*, 2018, **1**, 4900–4909.

21 S. Sarker, N. C. D. Nath, M. Rahman, S.-S. Lim, A. Ahammad, W.-Y. Choi and J.-J. Lee, TiO_2 paste formulation for crack-free mesoporous nanocrystalline film of dye-sensitized solar cells, *J. Nanosci. Nanotechnol.*, 2012, **12**, 5361–5366.

22 M. A. Airo, Synthesis and characterisation of metal selenide nanocrystals for use in electronic devices, PhD thesis, University of the Witwatersrand, 2017.

23 S. Lee, S. Cha, Y. Myung, K. Park, I. H. Kwak, I. S. Kwon, J. Seo, S. A. Lim, E. H. Cha and J. Park, Orthorhombic $NiSe_2$ nanocrystals on Si nanowires for efficient photoelectrochemical water splitting, *ACS Appl. Mater. Interfaces*, 2018, **10**, 33198–33204.

24 L. F. E. Machogo, P. Tetyana, R. Sithole, S. S. Gqoba, N. Phao, M. Airo, P. M. Shumbula, M. J. Moloto and N. Moloto, Unravelling the structural properties of mixed-valence α- and β-AuSe nanostructures using XRD, TEM and XPS, *Appl. Surf. Sci.*, 2018, **456**, 973–979.

25 R. K. Sithole, L. F. E. Machogo, M. A. Airo, S. S. Gqoba, M. J. Moloto, P. Shumbula, J. Van Wyk and N. Moloto, Synthesis and characterization of Cu_3N nanoparticles using pyrrole-2-carbaldpropyliminato Cu(II) complex and $Cu(NO_3)_2$ as single-source precursors: the search for an ideal precursor, *New J. Chem.*, 2018, **42**, 3042–3049.

26 S. Wang, W. Li, L. Xin, M. Wu, Y. Long, H. Huang and X. Lou, Facile synthesis of truncated cube-like $NiSe_2$ single crystals for high-performance asymmetric supercapacitors, *Chem. Eng. J.*, 2017, **330**, 1334–1341.

27 Y. Tian, Y. Ruan, J. Zhang, Z. Yang, J. Jiang and C. Wang, Controllable growth of NiSe nanorod arrays *via* one-pot hydrothermal method for high areal-capacitance supercapacitors, *Electrochim. Acta*, 2017, **250**, 327–334.

28 I. H. Kwak, H. S. Im, D. M. Jang, Y. W. Kim, K. Park, Y. R. Lim, E. H. Cha and J. Park, $CoSe_2$ and $NiSe_2$ nanocrystals as superior bifunctional catalysts for electrochemical and photoelectrochemical water splitting, *ACS Appl. Mater. Interfaces*, 2016, **8**, 5327–5334.

29 H. Chen, M. Fan, C. Li, G. Tian, C. Lv, D. Chen, K. Shu and J. Jiang, One-pot synthesis of hollow NiSe–CoSe

nanoparticles with improved performance for hybrid supercapacitors, *J. Power Sources*, 2016, **329**, 314–322.

30 A. T. Swesi, J. Masud and M. Nath, Nickel selenide as a high-efficiency catalyst for oxygen evolution reaction, *Energy Environ. Sci.*, 2016, **9**, 1771–1782.

31 X. Du, O. Lytken, M. S. Killian, J. Cao, T. Stubhan, M. Turbiez, P. Schmuki, H.-P. Steinrück, L. Ding, R. H. Fink, N. Li and C. J. Brabec, Overcoming interfacial losses in solution-processed organic multi-junction solar cells, *Adv. Energy Mater.*, 2016, 1601959.

32 J. Dong, J. Wu, J. Jia, J. Ge, Q. Bao, C. Wang and L. Fan, A transparent nickel selenide counter electrode for high efficient dye-sensitized solar cells, *Appl. Surf. Sci.*, 2017, **401**, 1–6.

33 V. Murugadoss, J. Lin, H. Liu, X. Mai, T. Ding, Z. Guo and S. Angaiah, Optimizing graphene content in a NiSe/graphene nanohybrid counter electrode to enhance the photovoltaic performance of dye-sensitized solar cells, *Nanoscale*, 2019, **11**, 17579–17589.

34 Y. Hou, D. Wang, X. H. Yang, W. Q. Fang, B. Zhang, H. F. Wang, G. Z. Lu, P. Hu, H. J. Zhao and H. G. Yang, Rational screening low-cost counter electrodes for dye-sensitized solar cells, *Nat. Commun.*, 2013, **4**, 1583.

35 S. Huang, Q. He, W. Chen, J. Zai, Q. Qiao and X. Qian, 3D hierarchical FeSe$_2$ microspheres: controlled synthesis and

applications in dye-sensitized solar cells, *Nano Energy*, 2015, **15**, 205–215.

36 C. Schuster, M. Gatti and A. Rubio, Electronic and magnetic properties of NiS$_2$, NiSSe and NiSe$_2$ by a combination of theoretical methods, *Eur. Phys. J. B*, 2012, **85**, 325.

37 G. Yue, W. Wu, X. Liu and H. Zheng, Enhanced photovoltaic performance of dye-sensitized solar cells based on a promising hybrid counter electrode of CoSe$_2$/MWCNTs, *Sol. Energy*, 2018, **167**, 137–146.

38 H. Sun and Z.-S. Wang, Highly efficient dye-sensitized solar cells with NiSe$_2$ counter electrodes: Effect of morphology on the electrocatalytic activity and the photovoltaic performance, *Chin. Sci. Bull.*, 2016, **62**, 1500–1506.

39 H. Sun, L. Zhang and Z.-S. Wang, Single-crystal CoSe$_2$ nanorods as an efficient electrocatalyst for dye-sensitized solar cells, *J. Mater. Chem. A*, 2014, **2**, 16023–16029.

40 C. Bao, F. Li, J. Wang, P. Sun, N. Huang, Y. Sun, L. Fang, L. Wang and X. Sun, One-pot solvothermal *in situ* growth of 1D single-crystalline NiSe on Ni foil as efficient and stable transparent conductive oxide free counter electrodes for dye-sensitized solar cells, *ACS Appl. Mater. Interfaces*, 2016, **8**, 32788–32796.

41 Z. Ning, Y. Fu and H. Tian, Improvement of dye-sensitized solar cells: what we know and what we need to know, *Energy Environ. Sci.*, 2010, **3**, 1170–1181.